Combined Neutron Diffraction and Atomistic Modeling Studies of Structure, Defects, and Water Incorporation in Doped Barium Cerate Perovskites

A. Kruth,[†,‡] R. A. Davies,[§] M. S. Islam,[||] and J. T. S. Irvine*[,†]

School of Chemistry, University of St. Andrews, St. Andrews, KY16 9ST, Scotland, United Kingdom, Materials Chemistry Group, Chemistry Division, University of Surrey, Guildford GU2 7XH, United Kingdom, and Department of Chemistry, University of Bath, Bath BA2 7AY, United Kingdom

Received October 13, 2006. Revised Manuscript Received January 3, 2007

A series of co-doped barium cerate perovskites, $Ba_{1-x}La_xCe_{0.9-x}Y_{0.1+x}O_{2.95}$, with $0 \leq x \leq 0.15$, was prepared by solid-state reaction, and the structural properties were investigated using high-resolution neutron diffraction. All compositions were found to exhibit the orthorhombic *Pbnm* structure, although the octahedral basal plane distortion is greatly reduced on doping, accompanied with an increase in octahedral elongation. Compositions close to the solid solution limit, $x = 0.1$ and 0.15, are pseudo-tetragonal and pseudo-cubic and appear to be close to a phase transition, most likely to space groups *Imma* or *I*4/*mcm*. An anomaly in unit cell parameters occurs at low dopant concentration, $0.03 \leq x \leq 0.05$, and was found to be reflected in reduction of the structural water uptake of the material within this compositional range. Atomistic simulations were carried out to study the energetics for dopant incorporation at A- and B-sites and water incorporation at oxygen sites. The results suggest that the reduced protonic defect concentration within the compositional range where the structural anomaly occurs might be caused by less favorable water incorporation energies.

Introduction

Barium cerate based perovskites exhibit high proton conductivities and are promising candidate electrolyte materials for protonic ceramic fuel cells.[1] Proton conduction occurs via the incorporation of protonic defects, $OH_O^{\cdot}$, at oxygen vacancies, $V_O^{\cdot\cdot}$, which can be created by aliovalent B-site doping of the parent composition $BaCeO_3$. Ce^{4+} is partially replaced by a lower valent cation, such as Y^{3+}, introducing acceptor dopant defects, Y_{Ce}', and giving compositions along the binary join $BaCe_{1-x}Y_xO_{3-x/2}$. Assuming that all cerium is present in valence state +4, the concentration of oxygen vacancies at high temperatures depends linearly on the Y content and can be increased to a maximum of 2.5% at $x = 0.15$. The extent of water incorporation at low temperatures in moist atmospheres has been found to be proportional to the concentration of oxygen vacancies.[2]

Oxide ion conduction has been observed to be closely related to structural properties such as octahedral tilting and disorder of oxygen sites,[3] and hence protonic diffusion and mobility are also likely to be limited by the degree of distortion of the perovskite structure due to $(Ce/Y)O_6$ octahedral tilting. Barium cerate perovskites show $GdFeO_3$-type tilting at low temperatures; however, the nature of octahedral tilting changes on heating, resulting in an unusual sequence of structural phase transitions: *Pmcn* to *Incn* to $F\bar{3}2/n$ to $Pm\bar{3}m$,[3−5] which can be expressed in the Glazer notation[4] as a $b^+a^-a^-$ to $b^0a^-a^-$ to $a^-a^-a^-$ to $a^0a^0a^0$ sequence of tilt systems. This sequence of phase transitions is most unusual because, at the $b^0a^-a^-$ to $a^-a^-a^-$ transition, octahedral tilting increases as the temperature is raised. The space group *Pmcn* has the standard setting *Pnma* (No. 62); however, another alternative setting for this space group is *Pbnm*, which is commonly used for perovskite systems. The metrics of the unit cell axes in *Pnma*, *Pbnm*, and *Pmcn* relate to each other as *xyz*, *zxy*, and *yzx*, respectively, with *x* being the unique axis (these settings correspond to $b^-a^+b^-$, $b^-b^-a^+$, and $a^+b^-b^-$ tilt systems in the Glazer notation). In this paper we use the *Pbnm* ($b^-b^-a^+$) setting throughout. While each of the settings is entirely valid, care must be taken to ensure that the two short axes are correctly identified as they are not symmetry equivalent.

The occurrence of non-protonic conduction such as electronic conduction as a result of reduction of Ce^{4+} to Ce^{3+} under reducing conditions would decrease the efficiency of the barium cerate-based fuel cell electrolyte materials. If the dopant ion is redox-stable, the reduction of Ce^{4+} to Ce^{3+} at high temperatures is likely to be accommodated by the formation of additional oxygen vacancies; however, the number of oxygen vacancies that can be accommodated in the perovskite is usually limited. The high oxidation state of 4+ for cerium may be stabilized by introducing a lower valence dopant ion such as Y^{3+} at the B-site. Charge

[†] University of St. Andrews.
[‡] Present address: Department of Chemistry, University of Aberdeen, Meston Walk, Aberdeen AB24 3UE, U.K.
[§] University of Surrey.
[||] University of Bath.

(1) Kreuer, K. D. *Solid State Ionics* **1997**, *97*, 1.
(2) Kruth, A.; Irvine, J. T. S. *Solid State Ionics* **2003**, *162−163*, 83.
(3) Bonanos, N.; Knight, K. S.; Ellis, B. *Solid State Ionics* **1995**, *79*, 161.
(4) Glazer, A. M. *Acta Crystallogr.* **1972**, *B28*, 3384.
(5) Liu, R. S.; Wu, J. B.; Chang, C. Y.; Lin, J. G.; Huang, C. Y.; Chen, J. M.; Liu, R. G. *J. Solid State Chem.* **1996**, *125*, 112.

10.1021/cm062448q CCC: $37.00
Published on Web 02/21/2007

compensation for such a doping mechanism occurs by creation of oxygen vacancies:

$$\frac{1}{2}Y_2O_3 + \frac{1}{2}O_O^{\times} + Ce_{Ce}^{\times} = Y'_{Ce} + \frac{1}{2}V_O^{\cdot\cdot} + CeO_2 \qquad (1)$$

This increase in oxygen vacancy concentration acts to oppose reduction of Ce^{4+} as described in following equation:

$$Ce_{Ce}^{\times} + \frac{1}{2}O_O^{\times} = Ce'_{Ce} + \frac{1}{2}V_O^{\cdot\cdot} + \frac{1}{4}O_2 \qquad (2)$$

Similarly, the valence state of Ce^{4+} can be reduced by introducing high valence ions at the A- or B-sites, comparable to the charge mechanism that occurs in GMR manganese perovskite materials, where the mixed oxidation state of manganese depends on the average A-cation valency.[5] Oxide ion conduction due to the presence of mobile oxygen vacancies occurs at high temperatures and also reduces fuel cell efficiency. In barium cerates, oxide ion transport was found to become significant in the rhombohedral $F\bar{3}2/n$ phase field where all oxygens are disordered.[3]

A further limitation to the application of barium cerate as an electrolyte material is its poor thermodynamic stability. Barium is known to volatize at high temperatures, forming amorphous barium oxide in the grain boundary regions, which can drastically lower the total conductivity of the material.[6,7] Small Ba losses leads to the formation of an A-cation deficient perovskite phase. At high Ba losses, the perovskite progressively decomposes into BaO, CeO_2, and Y_2O_3. In the presence of CO_2, loss of barium occurs more readily and the perovskite decomposes into $BaCO_3$, CeO_2, and Y_2O_3. At low CO_2 concentrations, however, barium cerate perovskites are stable above certain temperatures, for example, powdered samples of $BaCe_{0.9}Y_{0.1}O_{2.95}$ appeared to be stable up to 9% CO_2 in a CO_2/Ar gas mixture at temperatures above 750 °C.[8] Furthermore, dense barium cerate ceramics were found to be kinetically stable in CO_2 over long periods of time, for example, weeks, because the chemical reactions that are involved are interfacial.[6,9] In the presence of high steam concentrations, barium cerate perovskites decompose to form $Ba(OH)_2$, CeO_2, and Y_2O_3, which reflects the high solubility of protons in the material. Thermodynamic studies suggested that the high hydration enthalpy of barium cerate is a consequence of the high basicity of barium.[10]

This study is concerned with the relationship between dopant and oxygen vacancy concentration and properties such as structural distortion and water incorporation. For this purpose, $BaCe_{0.9}Y_{0.1}O_{2.95}$ was simultaneously doped with Y^{3+} at the B-site and La^{3+} at the A-site, giving compositions along the binary join $Ba_{1-y}La_yCe_{0.9-y}Y_yO_{2.95}$, and a constant nominal oxygen stoichiometry of 2.95 across the entire join. The Y^{3+} concentration at the B-site can be increased to a maximum of 25% at $y = 0.15$.[11] This substitution mechanism was chosen because increased disruption of the B-site cerium network will reduce the electronic mobilities and, neglecting any defect interaction, would be expected to maintain a constant vacancy content and hence a constant ionic conductivity.

X-ray diffraction (XRD) data presented in a previous report indicate that in both systems, $BaCe_{1-x}Y_xO_{3-x/2}$ and $Ba_{1-y}La_yCe_{0.9-y}Y_yO_{2.95}$, the general trends of unit cell parameters show significant deviations at low dopant contents.[11] This paper reports a detailed structural analysis using high-resolution neutron diffraction data and attempts to relate structural distortion mechanisms to the ability of the material to incorporate protonic defects. In addition, atomistic simulation techniques have been used to investigate the defect energetics of three systems: the undoped parent composition, $BaCeO_3$, and two doped systems, $BaCe_{0.9}Y_{0.1}O_{2.95}$ and $Ba_{0.9}La_{0.1}Ce_{0.8}Y_{0.2}O_{2.95}$. The simulation work focuses on dopant incorporation at A- and B-sites and water incorporation at oxygen vacancies. This work builds on previous simulation studies on proton-conducting perovskite oxides.[12,13]

Methods

Experimental Details. Powders of compositions along the binary join $Ba_{1-y}La_yCe_{0.9-x}Y_{0.1+x}O_{2.95}$ were prepared by solid-state reaction of $BaCO_3$, $Ce(NO_3)_3{\cdot}6H_2O$, Y_2O_3, and La_2O_3, as described elsewhere.[2,11] The final firing was carried out at 1450 °C for 2 days, and all samples were quenched from 1000 °C to room temperature.

Phase purity, nominal cation contents, and homogeneity were confirmed by XRD using a STOE Stadi P transmission diffractometer and by means of an EDX Inca Energy system, which was integrated within a JEOL JSM 5600 scanning electron microscope. The particle size of the powder was analyzed using a Coulter LS particle size analyzer and was found to be between 0.5 and 30 μm with approximately 80% of the particles having grain sizes between 10 and 30 μm.

For structural studies, time-of-flight (TOF) neutron powder diffraction data were collected on a high-resolution powder diffractometer, HRPD ($\Delta d/d_{max} = 1 \times 10^{-4}$) at ISIS, Rutherford Appleton Laboratory, over periods of 2−3 h. For each composition, approximately 1 cm^3 of the sample powder was contained in a thin-walled vanadium can. Backscattered data in the TOF range 35−115 ms were normalized to the incident monitor spectrum, corrected for detector efficiency using a vanadium diffraction pattern and re-binned to $\Delta d/d_{max} = 3 \times 10^{-4}$. Rietveld refinements were carried out using the General Structure Analysis System (GSAS).[14] First, the histogram scale factor, background, lattice parameters, and profile coefficients were refined, and after convergence of the profile refinement, the atomic coordinates and thermal vibration parameters of cations and anions and occupancies of the oxygens were refined.

(6) Chen, F.; Sørensen, O. T.; Meng, G.; Peng, D. *J. Mater. Chem.* **1997**, *3*, 481.
(7) Haile, S. M.; Staneff, G.; Ryu, K. H. *J. Mater. Sci.* **2001**, *36*, 1149.
(8) Zakowski, N.; Williamson, S.; Irvine, J. T. S. *Solid State Ionics* **2005**, *176*, 3019.
(9) Taniguchi, N.; Yasumoto, E.; Gamo, T. *J. Electrochem. Soc.* **1990**, *137*, 462.
(10) Kreuer, K. D.; Dippel, T.; Baikov, Y. M.; Maier, J. *Solid State Ionics* **1996**, *86*, 613.
(11) Kruth, A.; Mather, G. C.; Jurado, J. R.; Irvine, J. T. S. *Solid State Ionics* **2005**, *176*, 703.
(12) Glöckner, R.; Islam, M. S.; Norby, T. *Solid State Ionics* **1999**, *122*, 145.
(13) Davies, R. A.; Islam, M. S.; Gale, J. D. *Solid State Ionics* **1999**, *126*, 323.
(14) Von Dreele, R. B.; Larson, A. C. *General Structure Analysis System*; Laboratory Report LAUL 86-748, version 2001; Los Alamos National Laboratory: Los Alamos, NM, 1994.

The absorption coefficient was fixed during the early stages of the refinement but was refined after the first refinement of atomic coordinates and thermal parameters.

To investigate the amount of water that can be incorporated in the different compositions, as-prepared samples were first dried for 6 h in a Torvac-Centorr series 60 vacuum and controlled atmosphere furnace in a 0.05−0.1 mbar Ar atmosphere at 1100 °C. After cooling to room temperature, samples were immediately transferred into a RheoTherm thermogravimetric analysis (TGA) instrument and heated at 5 °C/min to 950 °C in a 3% H_2O/5% H_2/Ar atmosphere with the weight change recorded simultaneously. The samples were then held at 950 °C for 1 h and subsequently cooled at 5 °C/min.

Atomic Simulations. Only a short review of atomistic simulation techniques (embodied within the GULP code)[15] will be given here because comprehensive reviews have been given elsewhere.[16,17]

The basis of the lattice simulation was the specification of the potential energy of the system in terms of atomic coordinates. Both perfect and defect lattices were described by the Born model, in which the potential energy was partitioned into long-range Coulombic terms and short-range pair potentials of the Buckingham form:

$$V_{ij} = A_{ij} \exp\left(-\frac{r}{\rho_{ij}}\right) - \frac{C_{ij}}{r^6} \quad (3)$$

where the parameters A_{ij}, ρ_{ij}, and C_{ij} were assigned to interactions between ions of type i and ions of type j. The potential parameters used in this study were mostly taken from previous simulation studies.[17] The electronic polarizability which arises from charged defects in the lattice was also incorporated into the potential model via the shell model. The shell model has been shown to simulate effectively both dielectric and elastic properties of polar solids.

Lattice relaxation around a charge defect causes considerable perturbation of the surrounding lattice. The calculation of the energy associated with the defect was performed by the Mott-Littleton approach, in which the lattice is partitioned into inner and outer spherical regions centered on the defect. Ions in the inner region are relaxed explicitly, while the remainder of the crystal, where the defect forces are relatively weaker, relaxed by more approximate quasi-continuum methods. Mixed occupation of cation sites such as $BaCe_{0.9}Y_{0.1}O_{2.95}$ was modeled by employing a mean field approach where a hybrid B-atom was defined as having the weighted properties of $(1 - x)Ce^{4+}$ and xY^{3+}. The O−H interaction was modeled using an attractive Morse potential using parameters developed from ab initio quantum mechanical cluster calculations, with a point charge representation of the surrounding lattice. This approach has been employed successfully in previous studies of protons in perovskites.[12,13]

Errors. Unless otherwise stated, statistical errors or uncertainties are indicated by the last significant figure in both calculations and experimental measurements.

Results and Discussion

A. Structural Analysis of the $Ba_{1-x}La_xCe_{0.9-x}Y_{0.1+x}O_{2.95}$ Solid Solution. Neutron diffraction data for all compositions were refined in the *Pbnm* setting using the Rietveld method. Atomic positions and isotropic thermal parameters were refined for all atoms, whereas the site occupancies were refined only for the two oxygen sites, O1 and O2, and fixed for all cations. For all compositions $Ba_{1-x}La_xCe_{0.9-x}Y_{0.1+x}O_{2.95}$ ($0 \le x \le 0.15$), the refinement of site occupancy factors suggests that oxygen vacancies are preferably located at the equatorial O2 position. Figure 1 for example, shows Rietveld fits for compositions $x = 0.03$ and 0.10, with corresponding refined structural parameters such as atomic positions, cation and anion thermal parameters, and occupancies of oxygen sites shown in Tables 1 and 2. The small reflection at $d \sim 2.14$ Å corresponds to diffraction of the vanadium can that was used as the sample holder for the experiment.

The Rietveld fit between calculated and observed patterns was assessed using the statistical parameter, χ^2, called the "goodness of fit" or "agreement factor", for which $\chi = (R_{wp}/R_e)$. In Table 3, χ^2 factors are shown for all investigated compositions $0 \le x \le 0.15$. Values of χ^2 are ∼2 for low dopant levels and are slightly larger at higher dopant contents with $\chi^2 = 3.2$ at $x = 0.1$ and $\chi^2 = 4.8$ at $x = 0.15$. This suggests that the applied structural model, *Pbnm*, becomes inadequate at $x = 0.15$ and that this composition is near a phase transition. On closer inspection of the diffraction patterns from the 90° detector bank, the intensity of reflections that arises from in-phase octahedral tilting, for example, the superlattice reflections at $d = 2.304$ Å (at TOF = 81 ms) and 2.765 Å (at 96 ms), is greatly reduced for $x = 0.15$, although they are still present (Figure 2). It is likely that the material is close to a phase transition to a body-centered orthorhombic symmetry, space group *Imma*, resulting from $a^0b^-b^-$ tilting or, as the lattice parameters suggest pseudo-tetragonality, a tetragonal symmetry. According to the group−subgroup relationships for perovskites suggested by Howard and Stokes,[18] the only possible tetragonal space group with absence of in-phase octahedral tilting is *I*4/*mcm*, which is an $a^0a^0c^-$ tilt system. A similar phase sequence with the occurrence of pseudo-tetragonality within the orthorhombic phase field was, for instance, observed on heating in strontium zirconate by Howard et al.[19]

Isotropic A-cation and anion thermal parameters are shown in Figure 3 and compared with those reported by Knight for $BaCe_{0.9}Y_{0.1}O_{2.95}$ at room temperature (full symbols).[20,21] Observed thermal parameters are similar to the reported values, with A-cations and O1 and O2 exhibiting large values between 0.01 and 0.02 Å^2 and the B-cations having small thermal parameters of 0.001−0.005 Å^2. Parameters for the A-cation O1 and O2 positions show a general increase with x, with a discontinuity at $x \sim 0.05$, whereas the thermal parameter for the B-cation remains relatively constant between $0 \le x \le 0.1$ but is increased for composition $x = 0.15$.

An axial metric of $a > b$ was observed for compositions $0 \le x \le 0.05$, in agreement with the model used by Knight[22] for $BaCe_{0.9}Y_{0.1}O_{2.95}$. For high dopant levels at $0.07 \le x \le$

(15) Gale, J. D. *J. Chem. Soc., Faraday Trans.* **1997**, 629.
(16) Catlow, C. R. A. In *Solid State Chemistry: Techniques*; Cheetham, A. K., Day, P., Eds.; Clarendon Press: Oxford, 1987.
(17) Catlow, C. R. A., Ed. *Computer Modelling in Inorganic Crystallography*; Academic Press: San Diego, 1997.
(18) Howard, C. J.; Stokes, H. T. *Acta Crystallogr.* **1998**, *B54*, 782.
(19) Howard, C. J.; Knight, K. S.; Kennedy, B. J.; Kisi, E. H. *J. Phys.: Condens. Matter* **2000**, *12*, L677.
(20) Knight, K. S.; Soar, M.; Bonanos, N. *J. Mater. Chem.* **1992**, *2*, 709.
(21) Knight, K. S.; Bonanos, N. *Mater. Res. Bull.* **1995**, *30*, 347.
(22) Knight, K. S. *Solid State Ionics* **2001**, *145*, 275.

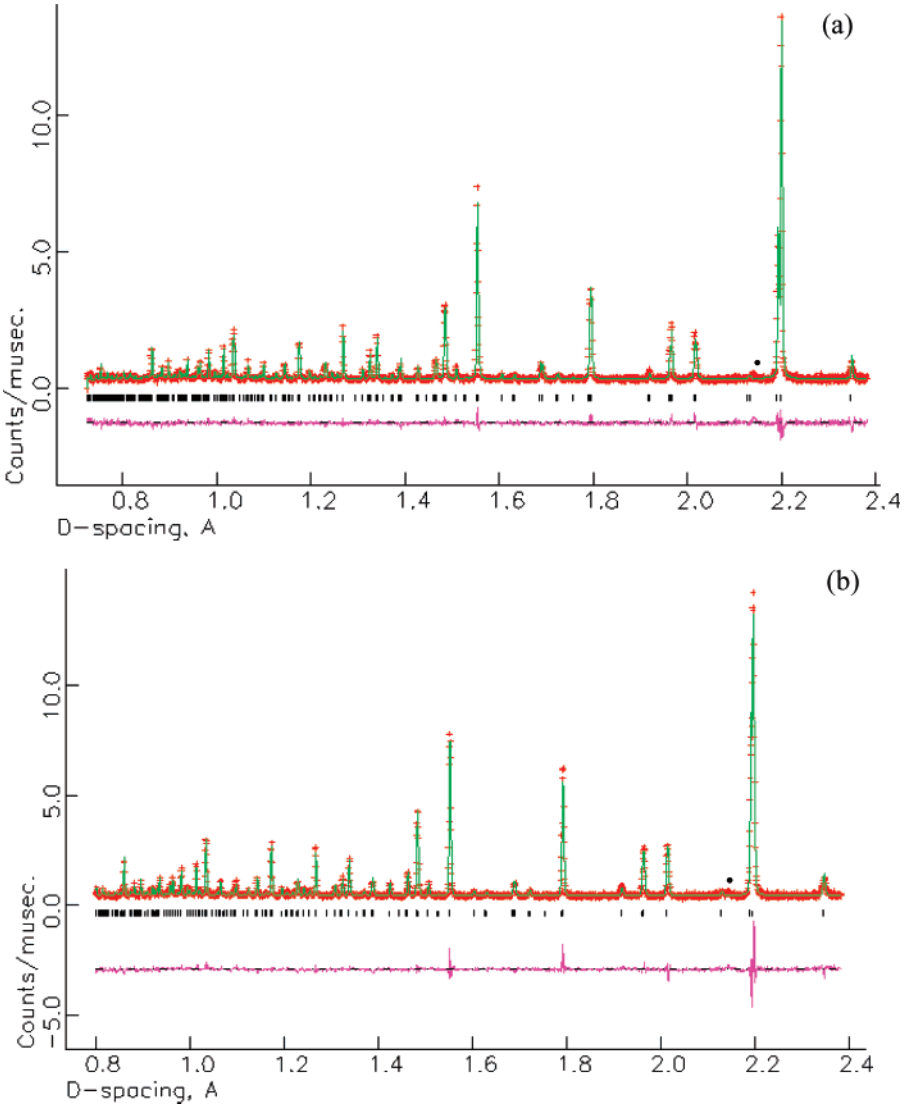

Figure 1. Rietveld fit of HRPD data for compositions (a) $Ba_{0.97}La_{0.03}Ce_{0.87}Y_{0.13}O_{2.95}$ (the weak reflection marked ● at $d \sim 2.14$ Å is due to the vanadium sample holder) and (b) $Ba_{0.93}La_{0.07}Ce_{0.83}Y_{0.17}O_{2.95}$.

Table 1. Atomic Coordinates, Occupancy of Oxygen Sites and Thermal Vibration Parameters for $Ba_{0.97}La_{0.03}Ce_{0.87}Y_{0.13}O_{2.95}$[a]

atom	Wyckoff position	occ.	*x*/*a*	*y*/*b*	*z*/*c*	100 × B_{iso}, Å^2
Ba	4c	0.97	0.0124(7)	−0.0019(9)	0.25	1.62(8)
La	4c	0.03	0.0124(7)	−0.0019(9)	0.25	1.62(8)
Ce	4b	0.87	0.5	0	0	0.15(6)
Y	4b	0.13	0.5	0	0	0.15(6)
O(1)	4c	0.99(2)	0.4907(9)	0.0760(5)	0.25	1.47(13)
O(2)	8d	0.96(1)	0.2732(4)	0.7257(4)	0.0410(2)	1.27(9)

[a] In *Pbnm* with $a = 6.2219(1)$ Å, $b = 6.2134(1)$ Å, and $c = 8.7667(1)$ Å, $R_p = 0.081$, $R_{wp} = 0.095$, and $\chi^2 = 1.2$

Table 2. Atomic Coordinates, Occupancy of Oxygen Sites, and Thermal Vibration Parameters for $Ba_{0.90}La_{0.10}Ce_{0.80}Y_{0.20}O_{2.95}$[a]

atom	Wyckoff position	occ.	*x*/*a*	*y*/*b*	*z*/*c*	100 × B_{iso}, Å^2
Ba	4c	0.90	0.0089(7)	0.0144(3)	0.25	1.49(4)
La	4c	0.10	0.0089(7)	0.0144(3)	0.25	1.49(4)
Ce	4b	0.80	0.5	0	0	0.22(3)
Y	4b	0.20	0.5	0	0	0.22(3)
O(1)	4c	1.01(2)	0.0795(5)	0.4886(4)	0.25	2.06(7)
O(2)	8d	0.91(1)	0.7278(3)	0.2742(2)	0.0430(2)	1.59(7)

[a] In *Pbnm* with $a = 6.1953(1)$ Å, $b = 6.1990(1)$ Å, $c = 8.7567(1)$, $R_p = 0.0867$, $R_{wp} = 0.1090$, and $\chi^2 = 3.2$.

Table 3. Agreement Factors, χ^2, for Rietveld Fits of $Ba_{1-x}La_xCe_{0.9-x}Y_{0.1+x}O_{2.95}$ in Space Group *Pbnm*

x	0	0.02	0.03	0.04	0.05	0.06	0.07	0.1	0.15
χ^2	1.88	2.27	1.21	2.41	1.95	2.36	1.57	3.25	4.83

0.15, values of *a* and *b* become very close to equal and even suggest a lattice metric of $a < b$. The significance of this change in lattice metrics will be discussed below.

Refined unit cell parameters are in good agreement with parameters observed in a previous XRD study,[10] showing a deviation from their general trends at intermediate values of *x*, Figure 4a. This indicates that the lattice is greatly elongated along *a* in $BaCe_{0.9}Y_{0.1}O_{2.95}$ and that this elongation is reduced on doping. Figure 4b shows the orthorhombic strain, ϵ, that was calculated from the unit cell parameters according to eq A1 (see Appendix). At low values of *x*, ϵ has a large negative value. This indicates that the BO_6 octahedra are highly distorted (tilting of regular octahedra around the *b*-axis would result in a positive orthorhombic strain).[5] On doping, ϵ increases until a small positive value is observed for $x \geq 0.07$. The calculated Ce/Y−O−Ce/Y bond angles in Figure 5 show that in $BaCe_{0.9}Y_{0.1}O_{2.95}$ ($x = 0$), axial Ce/Y−O1−Ce/Y and equatorial Ce/Y−O2−Ce/Y bonds are significantly

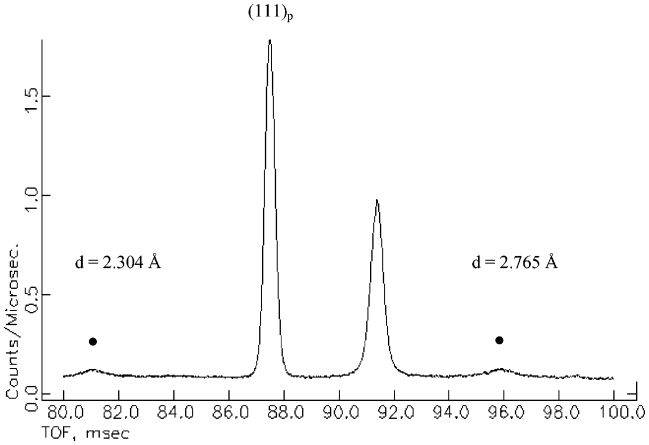

Figure 2. Superlattice reflection due to anti-phase octahedral tilting (marked with ●) in 90° HRPD data for $Ba_{0.85}La_{0.15}Ce_{0.75}Y_{0.25}O_{2.95}$.

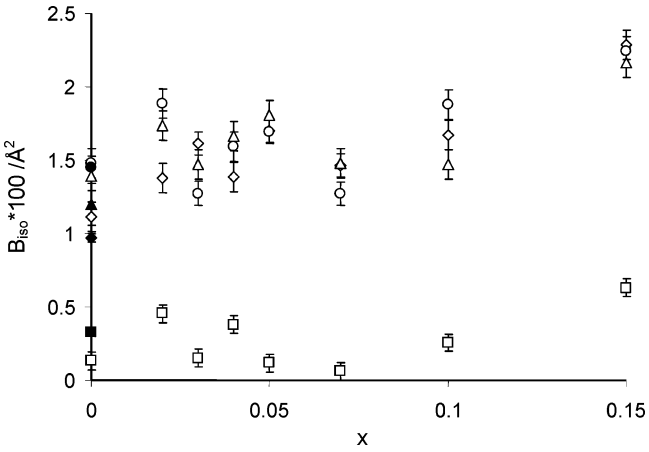

Figure 3. Thermal parameters for (◇) A- and (□) B-cations and (△) O1 and (○) O2 oxygen positions in $Ba_{1-x}La_xCe_{0.9-x}Y_{0.1+x}O_{2.95}$. Superimposed are parameters reported by Knight (full symbols).

distorted from 180°, with the axial bonds showing the largest deviation. This indicates that octahedra rotate more about the $[001]_p$ direction (corresponding to the *c*-axis in *Pbnm*) than they rotate about $[100]_p$ and $[010]_p$, giving a net octahedral tilt in the $(110)_p$ plane (corresponding to the *ab* plane in *Pbnm*). In the Glazer notation, this corresponds to a metric of rotation angle magnitudes $a > b$, for tilt system $b^-b^-a^+$ (where these are magnitudes of the rotation angles about the $[100]_p$, $[010]_p$, and $[001]_p$ directions). At $x = 0$, the equatorial Ce/Y−O2-Ce/Y bond angle is approximately 160°. For $x = 0.05$, the equatorial bond angle decreases, indicating that the magnitude of octahedral tilting in the $(110)_p$ plane is increased. For the same composition, the equatorial bond angle reaches a minimum of approximately 157.5° and, on further doping, this angle increases, indicating that octahedral tilting in the *ab* plane is again reduced. At $x = 0.15$, the bond angle regains the value of 160°, suggesting that the degrees of octahedral tilting in the *ab* plane are similar for the two solid solution end members, $x = 0$ and $x = 0.15$, although it was much increased for intermediate values of *x*. Axial Ce/Y−O1−Ce/Y bond angles, which give information about the magnitude of octahedral rotation in the $[001]_p$ direction (i.e., the *c*-axis), generally show a continuous decrease from 156 to 154° at compositions $x = 0$ and 0.15, respectively, although a small deviation at $x = 0.03-0.05$ is apparent.

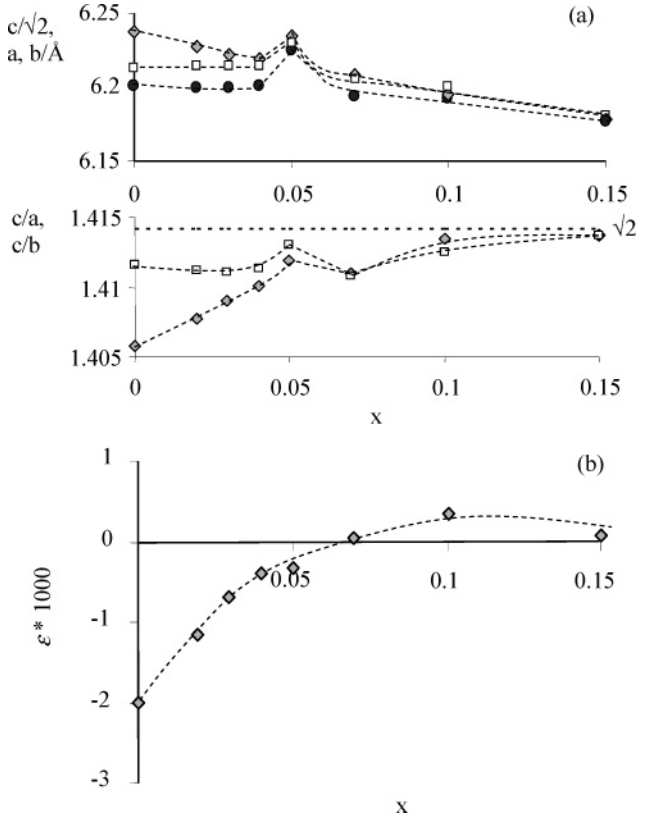

Figure 4. (a) Comparison of unit cell parameters: *a* or */a* (◆), *b* or *c*/*b* (□), and $c/\sqrt{2}$ (●). (b) Orthorhombic strain, ϵ, in $Ba_{1-x}La_xCe_{0.9-x}Y_{0.1+x}O_{2.95}$ solid solution.

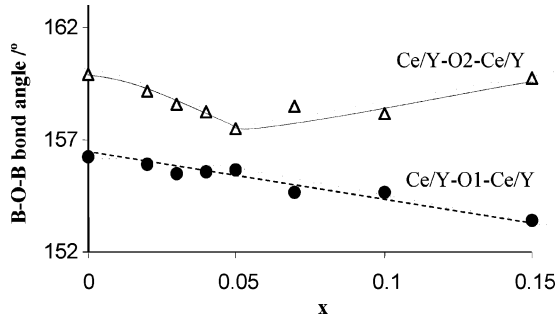

Figure 5. Variation of Ce/Y−O−Ce/Y bond angles in the $Ba_{1-x}La_xCe_{0.9-x}Y_{0.1+x}O_{2.95}$ join: (●) axial Ce/Y−O1−Ce/Y and (△) equatorial Ce/Y−O2−Ce/Y bonds.

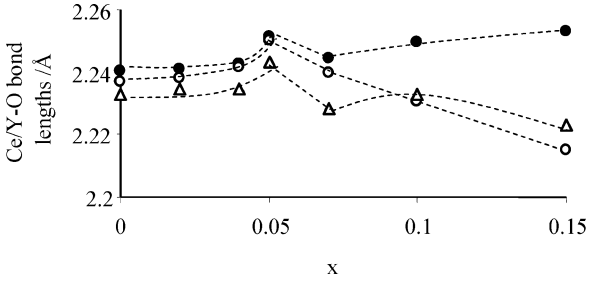

Figure 6. B−O bond lengths in $Ba_{1-x}La_xCe_{0.9-x}Y_{0.1+x}O_{2.95}$. B−O1, ●, and B−O2, ○ and △.

Calculated B−O bond lengths are shown in Figure 6. In $BaCe_{0.9}Y_{0.1}O_{2.95}$, the axial Ce/Y−O1 bond (full symbol) and the two equatorial Ce/Y−O2 bonds (open symbols) are almost equal; however, the Ce/Y-O1 bond is slightly longer than the Ce/Y−O2 bonds. This suggests that the elongation of octahedra along the *c*-axis that is usually encountered

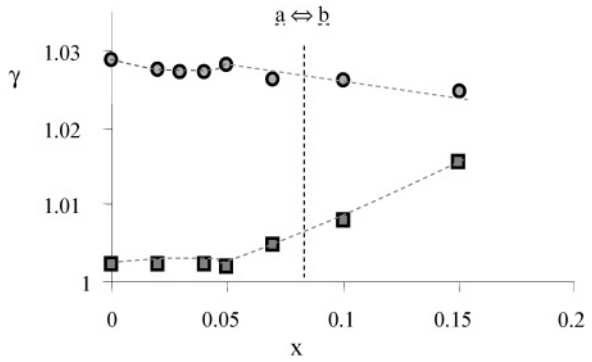

Figure 7. Octahedra deformation in $Ba_{1-x}La_xCe_{0.9-x}Y_{0.1+x}O_{2.95}$: ●, γ_{O2-O2}; □, γ_{B-O}.

Table 4. Calculated and Experimental (This Study) Unit Cell Parameters and Degrees of Tetragonality and Orthorhombicity

	$BaCeO_3$		$BaCe_{0.9}Y_{0.1}O_{2.95}$		$Ba_{0.9}La_{0.1}Ce_{0.8}Y_{0.2}O_{2.95}$	
	calcd	exptl	calcd	exptl	calcd	exptl
a, Å	6.2422	6.2347(1)	6.2371	6.2376(1)	6.2106	6.1952(1)
b, Å×d6	6.2304	6.2153(1)	6.2275	6.2125(1)	6.1854	6.1994(1)
c, Å	8.8179	8.7763(1)	8.8045	8.7690(1)	8.7676	8.7562(1)
a/*b*	1.0018	1.0031	1.0015	1.0040	1.0041	0.9993
$\sqrt{2}a/c$	1.0011	1.0047	1.0018	1.0060	1.0018	1.0006

because of rotation about the *c*-axis is very small. On doping, initially bond lengths increase until one of the equatorial Ce/Y−O2 bonds becomes almost equal to the axial bond at $x = 0.05$. At higher doping levels ($x > 0.05$) the trend drastically changes and Ce/Y−O bonds increasingly diverge—the axial bond increases and equatorial bonds decrease.

Figure 7 shows the calculated octahedral deformation, namely, the octahedral elongation γ_{BO}, arising from nonequality of axial and equatorial bond lengths, and the octahedral basal plane deformation, γ_{O2-O2}, from the nonequality of the basal plane edges (see Appendix for details of calculation). For $0 \le x \le 0.05$, the basal plane distortion, γ_{O2-O2}, is significant, because of large splitting of the O2−O2 edge lengths (which differ by almost 3%). The octahedral elongation is small, as indicated by γ_{BO} being close to 1. Interestingly, γ_{O2-O2} and γ_{BO} appear to be constant over the compositional range, $0 \le x \le 0.05$. At higher doping levels, $x > 0.05$, γ_{O2-O2} decreases, whereas γ_{B-O} increases, both in continuous manners.

These results suggest that two competing distortion mechanisms occur over the compositional range $0 \le x \le 0.15$ in $Ba_{1-x}La_xCe_{0.9-x}Y_{0.1+x}O_{2.95}$. First, octahedra may be elongated along the *c*-axis, which results from the rotation about the $[001]_p$ direction. This distortion is usually observed in $GdFeO_3$-type perovskite oxides. Second, a deformation of the octahedral basal plane may occur which was found to be associated with an increased net octahedra tilting in the $(110)_p$ plane. For low dopant levels, $0 \le x \le 0.05$, the deformation of the octahedral plane is the dominating mechanism, indicated by large γ_{O2-O2} and a negative orthorhombic strain. Such intrinsic distortion of the octahedra also occurs, for instance, in the primitive orthorhombic perovskite $LaTiO_3$.[23] At high doping levels, $x > 0.05$, octahedral elongation increases and becomes more dominant.

The interatomic potential model was used to simulate the structures of three selected compositions, $BaCeO_3$, $BaCe_{0.9}Y_{0.1}O_{2.95}$, and $Ba_{0.9}La_{0.1}Ce_{0.8}Y_{0.2}O_{2.95}$ (hereafter referred to as "BC", "BCY", and "BLCY", respectively). In Table 4, the calculated unit cell parameters are compared with observed parameters. For all three systems, the calculated parameters are in fairly good agreement and within 1% of the experimental values, although a convergence in magnitude of the two short unit cell axes in BLCY was not observed in the simulated structure. It is worth noting, however, that the calculated data necessarily relate to unhydrated lattices, while the experimental data relate to samples that would have contained some lattice water.

B. Water Incorporation in the $Ba_{1-y}La_yCe_{0.9-y}Y_{0.1+x}O_{2.95}$ System. Hydration and dehydration studies of the $BaCe_{1-x}Y_xO_{3-x/2}$ solid solution (including $BaCe_{0.9}Y_{0.1}O_{2.95}$, one of the parent compositions of the $Ba_{1-x}La_xCe_{0.9-x}Y_{0.1+x}O_{2.95}$ system) were reported previously.[2] A linear relationship between the maximum amount of water that can be incorporated and the nominal oxygen vacancy concentration in $BaCe_{1-x}Y_xO_{3-x/2}$ was observed, suggesting that water incorporation depends predominantly on oxygen vacancy concentration (in fully hydrated materials around 80% of nominal oxygen vacancies are occupied by protonic defects). From this, one can expect that in a system which has a constant nominal oxygen vacancy concentration across the whole solid solution range, such as $Ba_{1-y}La_yCe_{0.9-y}Y_{0.1+x}O_{2.95}$ with $[V_O] = 0.05$, the maximum amount of water that can be incorporated also remains constant, regardless of the dopant concentration.

Weight changes during hydration and dehydration of $Ba_{1-x}La_xCe_{0.9-x}Y_{0.1+x}O_{2.95}$ were investigated for a number of compositions over the range $0 \le x \le 0.15$. At high dopant levels ($x > 0.05$) weight traces and magnitude of weight change are very similar to those of $BaCe_{0.9}Y_{0.1}O_{2.95}$[2] as shown in Figure 8a. This result implies that water uptake depends predominantly on the number of oxygen vacancies rather than the dopant concentration, in agreement with previous observations. The weight traces for low dopant concentrations (Figure 8b), however, show that the maximum water uptake is greatly reduced for compositions $0.02 \le x \le 0.05$, up to 50% at $x = 0.05$. The variation of the maximum amount of water that could be incorporated into the structure at different dopant contents, *x*, is shown in Figure 9. The compositional region where water uptake is reduced is identical with that where the unit cell parameters deviate from their general trends reflecting that water incorporation has direct consequences on structural distortions. To determine the possible cause for the reduction of water uptake, and therefore in protonic defect concentration, in compositions $0.02 \le x \le 0.05$, many factors have to be considered, which are discussed in a later section.

An additional set of experiments was carried out to investigate the influence of the microstructure on the degree and rate of hydration and dehydration. In Figure 10, the weight trace of a powdered and initially dehydrated sample with composition $x = 0.15$ and an average particle size of 15−20 μm is superimposed on that of a dehydrated sintered

(23) Cwik, M.; Lorenz, T.; Baier, J.; Müller, R.; André, G.; Bourée, F.; Lichtenberg, F.; Freimuth, A.; Müller-Hartmann, E.; Braden, M. *Phys. Rev. B* **2003**, *68*, 060401.

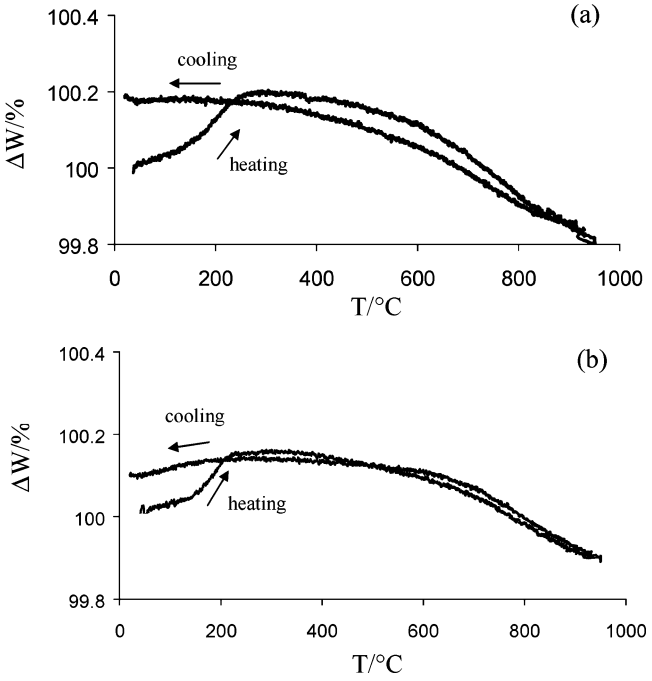

Figure 8. TGA traces for dehydrated (a) $Ba_{0.85}La_{0.15}Ce_{0.75}Y_{0.25}O_{2.95}$ and (b) $Ba_{0.95}La_{0.05}Ce_{0.85}Y_{0.15}O_{2.95}$ on heating and cooling in 3% H_2O/5% H_2/Ar.

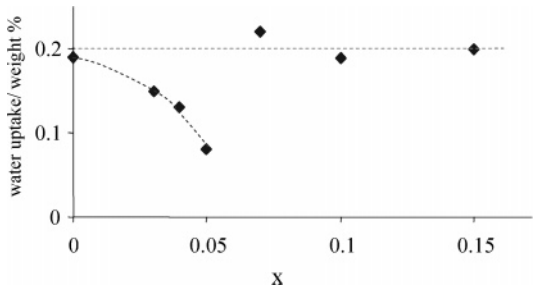

Figure 9. Variation of maximum water uptake with dopant content, x, in $Ba_{1-x}La_xCe_{0.9-x}Y_{0.1+x}O_{2.95}$.

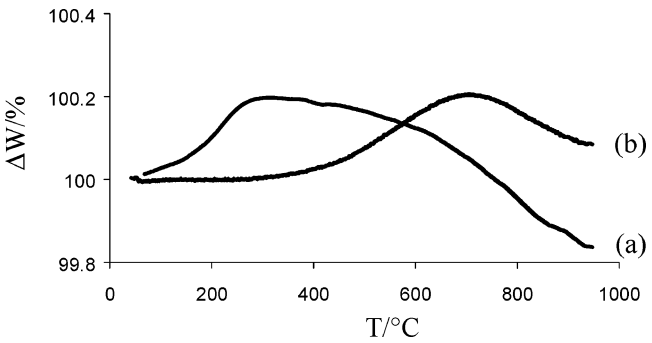

Figure 10. Comparison of hydration traces for initially dehydrated samples with composition $x = 0.15$ but with different microstructures: (a) a powdered sample with a particle size of 15−20 μm and (b) a sintered specimen with a density of 80%.

pellet (with a calculated density of ca. 80% of the theoretical value) of the same composition. Both samples were heated under the same conditions (as described in the experimental section). For the sintered sample, the water uptake commences at significantly higher temperature, and maximum hydration is achieved at about 750 °C as compared to ∼300 °C for the powdered sample; however, the amount of water that can be incorporated is similar for both samples, that is, ∼0.2 wt %. This suggests that although the microstructure has a significant effect on the kinetics of water uptake and loss, the maximum degree of hydration appears to be independent of microstructure for the methods used here.

Using atomistic simulation techniques, the energetics of water incorporation were calculated for the three systems BC, BCY, and BLCY. As mentioned in the introduction, mobile protons are incorporated into the perovskite structure on substitution of oxygen vacancies with hydroxyl groups according to reaction 1. The enthalpy of water dissolution (proton incorporation), E_{H_2O}, for the proton-conducting perovskites is known to be exothermic so that the ionic conductivity is dominated by protons at low temperatures and oxygen vacancies at high temperatures.

The same methodology used previously for evaluating the energetics of water incorporation in HTPC perovskites[12,13] was employed here to calculate E_{H_2O} for the incorporation of protonic defects at the two crystallographic oxygen sites, O1 and O2, according to

$$E_{H_2O} = 2E_{OH} + E_{V_O^{\cdot\cdot}} + E_{PT} \quad (4)$$

where E_{H_2O} is the water incorporation energy, E_{OH} and $E_{V_O^{\cdot\cdot}}$ are defect energies for an isolated protonic defect and an oxygen vacancy, respectively, and E_{PT} is the energy of the gas-phase reaction $O^{2-} + H_2O = 2OH^-$.

The CeO_6-octahedra network in $BaCeO_3$ and calculated position of a proton attached to either an axial or an equatorial oxygen are shown in Figure 11. When the protonic defect is located near the axial O1 position, it relaxes to a position that forms a Ce−O1−H angle of approximately 90°, whereas if positioned near the equatorial O2 site, the Ce−O2−H angle is approximately 45°. The calculated H−O2 and H−O1 bond lengths were 0.98 Å in both cases in accordance with spectroscopic values. The position of the proton attached to O2 is in good agreement with the proton position that was observed in a neutron diffraction study by Knight[24] of protonated $BaCe_{0.9}Y_{0.1}O_{2.95}$ in which two possible positions for the hydrogen close to O2 were considered, but only one position remained stable during refinement. The first (unstable) position formed a Ce−O2−H angle of approximately 90°, corresponding to a H−O2 separation of 1.48 Å. For the second position (which remained stable during the refinement), the Ce−O2−H angle was ∼45°, and the H−O2 bond length was 0.93 Å. This is in good agreement with our calculations for protonic defects located at O2.

The calculated values for E_{H_2O} after relaxation (for water incorporation at O1 and O2 sites) are listed in Table 5. Calculated values indicate a negligible difference in defect energies for oxygen vacancies located at O1 and O2 for all three compositions, which suggests similar oxygen vacancy concentrations at both sites. This differs from results from neutron refinements which suggest that oxygen vacancies in BCY are predominantly incorporated at the equatorial O2 position. Water incorporation energies are found to be

(24) Knight, K. S. *Solid State Ionics* **2000**, *127*, 43.

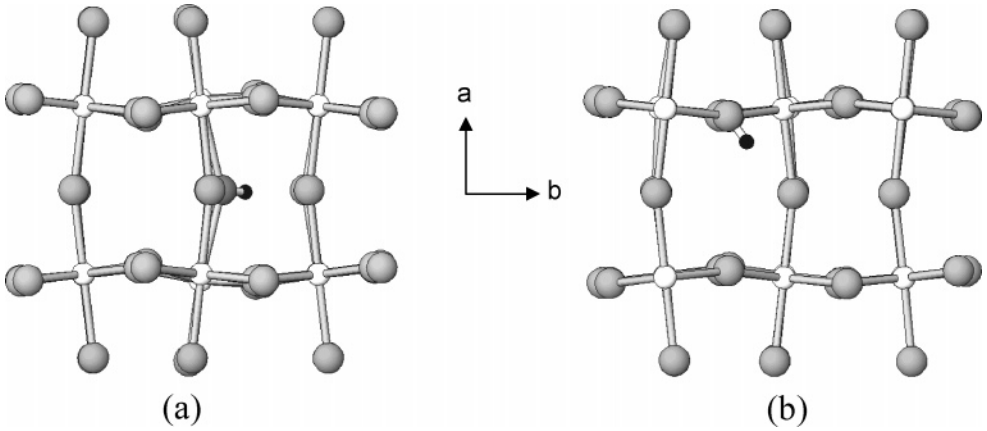

Figure 11. Relaxed position of the proton attached to (a) axial oxygen, O1, or (b) equatorial oxygen, O2, in $BaCeO_3$.

Table 5. Water Incorporation Energies (E_{H_2O}) for BC, BCY, and BLCY for $OH^{\cdot}$ at O1 and O2 Sites

	E_{H_2O}, eV per defect		
defect site	BC	BCY	BLCY
$OH^{\cdot}_{O1}$	−1.71	−1.97	−2.90
$OH^{\cdot}_{O2}$	−0.82	−2.80	−2.42

negative for BC, BCY, and BLCY, indicating that, in all three compositions, hydration of oxygen vacancies is exothermic and energetically favorable. Literature values for the enthalpy of water dissolution in $BaCeO_3$-based systems, for example, for BCY (in its cubic high-temperature polymorph),[12] correspond well with our calculated values. With increasing oxygen vacancy concentration, that is, comparing BC and BCY, E_{H_2O} decreases for both oxygen sites, O1 and O2, suggesting that hydration becomes increasingly exothermic and occurs even more readily when the oxygen vacancy concentration is increased. This is also in agreement with the results of Glöckner et al.[12] Comparing the calculated values for BCY and BLCY which have similar oxygen vacancy concentrations, however, we find that different trends in energetics are observed for protons attached to O1 and O2: E_{H_2O} becomes even more exothermic on Y/La-codoping when the proton is attached to an oxygen on the O1 position, whereas E_{H_2O} is less exothermic for a proton located near the O2 position.

For BCY with a high density of oxygen vacancies, E_{H_2O} is more exothermic for water incorporation at the O2 position. This is in agreement with neutron diffraction studies on this composition.[24] For BLCY, the trend is reversed and proton incorporation at the O1 site is more exothermic than on the O2 site. More importantly, assuming that the trends of the water incorporation energies between compositions BCY and BLCY are continuous, a compositional crossover region must exist where E_{H_2O} is equal for the O1 and O2 sites and much less exothermic than in BCY and BLCY. This region appears to occur near $x \sim 0.05$, where the water uptake is reduced by 50% and where unit cell parameters show deviations from Vegard's law, which are assumed to arise from differences in water content.

C. Dopant Substitution. The substitution of trivalent cations was investigated on both the A- and the B-sites for BC, BCY, and BLCY in order to gain some insight into the relative energetics of dopant incorporation. Substitution of the trivalent cation on the Ce site was analyzed according to the standard "acceptor-doping" defect reaction, with the creation of oxygen vacancies as charge-compensating defects:

$$\frac{1}{2}M_2O_3 + Ce_{Ce}^{\times} + \frac{1}{2}O_O^{\times} = M'_{Ce} + CeO_2 + \frac{1}{2}V_O^{\cdot\cdot} \qquad (5)$$

For substitution on the Ba-site, two possible compensation mechanisms were investigated, corresponding to the creation of cation vacancies

$$\frac{3}{2}Ba_{Ba}^{\times} + \frac{1}{2}M_2O_3 = M_{Ba}^{\cdot} + \frac{1}{2}V''_{Ba} + \frac{3}{2}BaO(s) \qquad (6)$$

and the consumption or filling of oxygen vacancies in the doped system

$$\frac{1}{2}M_2O_3 + Ba_{Ba}^{\times} + \frac{1}{2}V_O^{\cdot\cdot} = M_{Ba}^{\cdot} + BaO(s) + \frac{1}{2}O_O^{\times} \qquad (7)$$

The energies of the above reactions were evaluated by combining the corresponding defect and lattice energy terms.[25] This provides a systematic analysis of the relative energies of different dopant species on the same site and, in the case of substitution on the A-site, of the preferred compensation mechanism. The interatomic potentials for the dopant cations were taken as those corresponding to the binary metal oxides.[25] The resulting solution energies for substitution on the A- and B-sites for BC, BCY, and BLCY are listed in Table 6. Several interesting observations may be made from the results (we note our focus on trends rather than the absolute values because of uncertainties in the magnitude of the lattice energies employed). For A-site doping, the calculated solution energies are much smaller when the dopant defects are compensated by filling of oxygen vacancies (eq 7) than when compensation occurs by formation of A-site vacancies (eq 6). From this, defect mechanism 7 appears to be energetically more favorable. For mechanism 6, E_{sol} for A-site dopants increases in the order $La^{3+} < Y^{3+} < Ce^{3+}$, and for mechanism 7, E_{sol} is also larger for Y^{3+} than La^{3+}. La^{3+} is clearly the preferred dopant ion for the A-site in BC and BCY, but in BLCY, La^{3+} and Y^{3+}

(25) Cherry, M.; Islam, M. S.; Gale, J. D.; Catlow, C. R. A. *Solid State Ionics* **1995**, *77*, 207.

Table 6. Calculated Solution Energies for Dopants at A- and B-Sites in $BaCeO_3$, $BaCe_{0.9}Y_{0.1}O_{2.95}$, and $Ba_{0.9}La_{0.1}Ce_{0.8}Y_{0.2}O_{2.95}$

	energy per dopant, eV		
defect	BC	BCY	BLCY
	(a) Solution Energies for A-Site Doping According to Equation 6		
$La_{Ba}^{\cdot}$	4.03	4.10	3.55
$Y_{Ba}^{\cdot}$	4.22	4.27	3.56
$Ce_{Ba}^{\cdot}$	5.89	5.92	5.58
	(b) Solution Energies for A-Site Doping According to Equation 7		
$La_{Ba}^{\cdot}$	0.63	0.75	0.38
$Y_{Ba}^{\cdot}$	0.81	0.92	0.39
	(c) Solution Energies for B-Site Doping According to Equation 5		
La_{Ce}'	4.10	4.03	3.86
Y_{Ce}'	2.41	2.41	2.28
Ce_{Ce}'	3.98	3.90	3.75

have similar solution energies suggesting that they could both be equally incorporated at the A-site. For B-site doping via mechanism 5, E_{sol} is smallest for Y^{3+} and increases in the order $Y^{3+} < Ce^{3+} < La^{3+}$, suggesting that Y^{3+} is the most favorable dopant ion at the B-site in all three compositions, whereas La^{3+} incorporation is not favored at the B-site. This suggests incorporation of Y^{3+} at the A-site is energetically unfavorable in BC and BCY, whereas it is energetically possible in BLCY.

A shift of the B-site dopant ion to occupy the A-site is frequently observed in A-site deficient barium and strontium cerates[11,26−29] (where the A-site deficiency has been created by adjusting the nominal composition). Such dopant distribution over both A- and B-sites, according to $A_{0.9}B_{0.9}B'_{0.1}O_{2.85} \rightarrow A_{0.95}A'_{0.05}B_{0.95}B'_{0.05}O_3$, was observed to lead to a reduced oxygen vacancy concentration and hence reduced proton uptake and lower proton conductivity. In A-cation stoichiometric compositions, however, this process would necessitate a dissolution or evaporation of significant amounts of AO. Such evaporation or dissolution of Ba was not observed in the present system as samples were prepared at relatively low sintering temperatures of 1450 °C, and the stoichiometry and homogeneity of the samples were investigated and confirmed by scanning electron spectroscopy and energy-dispersive X-ray analysis. A reduction of the oxygen vacancy concentration as a result of such B-site dopant cross-substitution is hence unlikely to be the cause of the observed structural deviation and reduction of water uptake at a stoichiometry of $x \sim 0.05$ in $Ba_{1-x}La_xCe_{0.9-x}Y_{0.1+x}O_{2.95}$.

Finally, a partial switch-over of La and Y dopant ions in the composition $Ba_{0.9}La_{0.1}Ce_{0.9}Y_{0.1}O_{2.95}$ could occur; however, it has to be noted that if the incorporation of Y^{3+} at the B-site occurs to its full extent, then no Y^{3+} would be available for incorporation at the A-site. In addition, if Y^{3+} is incorporated at the A-site, then La^{3+} is likely to substitute at the B-site, according to $Y'_{Ce} + La_{Ba}^{\cdot} = Y_{Ba}^{\cdot} + La'_{Ce}$, which would have no effect on the oxygen vacancy concentration.

Conclusions

High-resolution neutron diffraction and atomistic modeling techniques were used to investigate a series of doped barium cerate proton conductors. In $BaCe_{0.9}Y_{0.1}O_{2.95}$, the octahedral basal plane is highly strained, and this strain can be released by co-doping with La^{3+} at the A-site to increase the Y^{3+} concentration at the B-site. The reduction of the basal plane distortion is accompanied by an increase in octahedral elongation
along the *c*-axis. Inconsistent variations of unit cell parameters, occurring over a small range of composition, indicate the existence of a structural anomaly. This structural anomaly was found to be reflected in an important physical property: the amount of water that can be incorporated into the structure is drastically reduced within the anomaly range. Defect energy calculations suggest a possible "switch-over" of La and Y dopants at high dopant contents in $Ba_{1-x}La_xCe_{0.9-x}Y_{0.1+x}O_{2.95}$. However, as this would have no influence on the oxygen vacancy concentration it is unlikely to be the primary cause of the observed behavior. The results suggest that the reduced protonic defect concentration within the compositional range where the structural anomaly occurs might be caused by less favorable water incorporation energies.

Acknowledgment. The authors would like to thank Dr. Richard Ibberson from ISIS for his support at HRPD, the EPSRC for a research grant, and the EPSRC Perovskite Network for travel support.

Appendix

Orthorhombic Distortion in $GdFeO_3$-Type Perovskite Oxides. *Octahedra Tilting.* The reduction of symmetry in $GdFeO_3$-type perovskite systems compared to the primitive cubic perovskite prototype occurs as a result of octahedra rotating about all three primitive cubic crystallographic axes, $[100]_p$, $[010]_p$, and $[001]_p$. While octahedra rotate in-phase about the $[001]_p$ axis (which corresponds to the *c*-axis in *Pbnm*), they rotate in an anti-phase manner about the other two axes, $[100]_p$ and $[010]_p$. Both anti-phase rotations result in a net anti-phase octahedra tilt along the $[110]_p$ axis (or *b*-axis in *Pbnm*).

The *Pbnm* primitive orthorhombic lattice parameters are derived from the primitive cubic unit cell where $a_{po} \sim b_{po} = \sqrt{2}a_p$ and $c_{po} = 2a_p$. Assuming that octahedra are regular, the non-equality $\sqrt{2}c_{po} \neq a + b$ arises from the rotation of the octahedra about $[001]_{pc}$ only, and the distortion $a \neq b$ is a result of the net tilt along $[110]_p$.[11] The orthorhombic distortion, ϵ, may be calculated from

$$\epsilon = \frac{b - a}{a + b} \tag{A1}$$

Tilting of ideal octahedra along the $[110]_p$ axis would lead to an axial metric of $b > a$ and a positive sign for ϵ. In pure

(26) Shima, D.; Haile, S. M. *Solid State Ionics* **1997**, *97*, 443.
(27) Mather, G. C.; Islam, M. S. *Chem. Mater.* **2005**, *17*, 1736.
(28) Wu, J.; Li, L. P.; Espinosa, L.; Haile, S. M. *J. Mater. Res.* **2004**, *19*, 2366.
(29) Wu, J.; Davies, R. A.; Islam, M. S.; Haile, S. M. *Chem. Mater.* **2005**, *17*, 846.

and doped barium cerate, the lattice metric is $a > b$, resulting in a negative sign for ϵ and indicating that the octahedra are non-regular (another example showing this behavior is ferroelectric $LaTiO_3$).[23]

Octahedra Deformation. Two main mechanisms for the deformation of octahedra can be distinguished. The deformation of the BO_6 octahedra can be associated with an elongation of the octahedra and thus a degeneration of B−O bond lengths (eq A2). A distortion of the octahedra basal plane is characterized by the non-equality of the basal plane edges (eq A3).

$$\gamma_{BO} = \frac{B - O_{long}}{B - O_{short}} \tag{A2}$$

$$\gamma_{O2-O2} = \frac{O2 - O2_{long}}{O2 - O2_{short}} \tag{A3}$$

CM062448Q